

# Plug-and-Play Continuous Gas Flow Assembly of Cysteine-Inserted AuCu Nanobimetal for Folate-Receptor-Targeted Chemo-Phototherapy

Bijay Kumar Poudel,<sup>†</sup> Jungho Hwang,<sup>\*,†</sup> Sae Kwang Ku,<sup>‡</sup> Jong Oh Kim,<sup>\*,§</sup> and Jeong Hoon Byeon<sup>\*,||</sup>

<sup>†</sup>School of Mechanical Engineering, Yonsei University, Seoul 03722, Republic of Korea

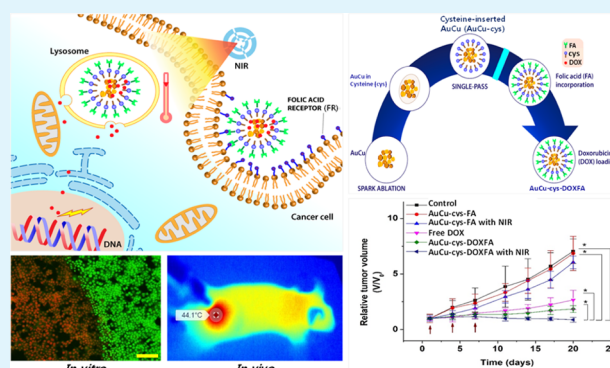
<sup>‡</sup>College of Korean Medicine, Daegu Haany University, Gyeongsan 38610, Republic of Korea

<sup>§</sup>College of Pharmacy and <sup>||</sup>School of Mechanical Engineering, Yeungnam University, Gyeongsan 38541, Republic of Korea

## Supporting Information

**ABSTRACT:** Conjugatable nanobimetal exhibiting broadband light absorption for use as phototherapeutic platforms were assembled via a plug-and-play continuous gas flow route. Electrically produced AuCu nanobunches (NBs) under nitrogen gas flow were directly injected into cysteine (cys) solution through gas pressurization to mechanically spray the solution (AuCu into cys droplets). The sprayed droplets were then exposed to 185 nm UV light (higher photon energy [6.2 eV] than the work functions of Au [5.1 eV] and Cu [4.7 eV]) to initiate photoionization of AuCu NBs for subsequent electrostatic reaction with the SH<sup>−</sup> group of cys to form cys-inserted AuCu (AuCu-cys) platforms in a single-pass gas stream. These platforms exhibited broadband light absorption spectra because of hybridized interparticle plasmonic coupling and could be conjugated to folic acid (FA) when dispersed in FA solution to form highly dispersible, biocompatible, and cancer-targetable AuCu-cys-FA. This material was suitable for use in targeted phototherapy of folate-receptor (FR)-rich cancers via FR-mediated endocytosis, and loading doxorubicin (DOX) into AuCu-cys-FA (i.e., AuCu-cys-DOXFA) facilitated chemo-phototherapy because of photoresponsive anticancer drug release upon induction of hyperthermia.

**KEYWORDS:** conjugatable nanobimetal, plug-and-play continuous gas flow route, AuCu nanobunches, folate-receptor, targeted chemo-phototherapy



Various biofunctional nanocomposites containing organic and inorganic components of various sizes, morphologies, structures, or compositions have been employed as stimuli-responsive cancer therapeutics controlled by application of external energy. Gold nanostructures (Au NSs), in particular, are composites that hold prospects for designing optoresponsive transducers with a wider control over their plasma properties (localized surface plasmon resonance [LSPR] and line-width) compared with the majority of their counterparts. Recently, Au-based bimetallic NSs have been used to generate broadband light absorption spectra by tuning their LSPRs based on combination with other metallic components.<sup>1–4</sup> Tuning the crystalline structure of bimetallic (e.g., Au and silver [Ag] or Au and copper [Cu]) NSs have also been used to control LSPR properties by using the linear relationship between the two components.<sup>5</sup> This tunable optical property coupled with the biocompatibility of Au means that Au-based nanobimetal could be employed in numerous therapeutic and diagnostic fields.<sup>6</sup> However, loading organic components (for targeting, probing, and/or as therapeutic agents) on the nanobimetal is essential for producing the highly selective,

permeable anti-invasive characteristics required for advanced biomedical applications.<sup>7–9</sup>

Even though these composites exhibit potential as advanced theranostics because of the synergistic effects of organic and inorganic material combinations, they face challenges posed by the harsh, costly, and hazardous batch-wise processes needed to produce them as the demand increases.<sup>10</sup> Specifically, preparing the composites requires multiple processes to produce the metallic nanostructures, to load the with targeting and therapeutic layers, and to purify, separate, and stabilize them in readiness for bioapplications. This also produces unwanted hazardous byproducts and wastes that pose human and environmental hazards; thus, development of a continuous flow process that enables scale-up and automation is needed to efficiently produce these composites.

More recently, the digitization of hydrothermal reactions for on-demand production of pharmaceuticals has been intro-

Received: February 4, 2019

Accepted: April 23, 2019

Published: April 23, 2019

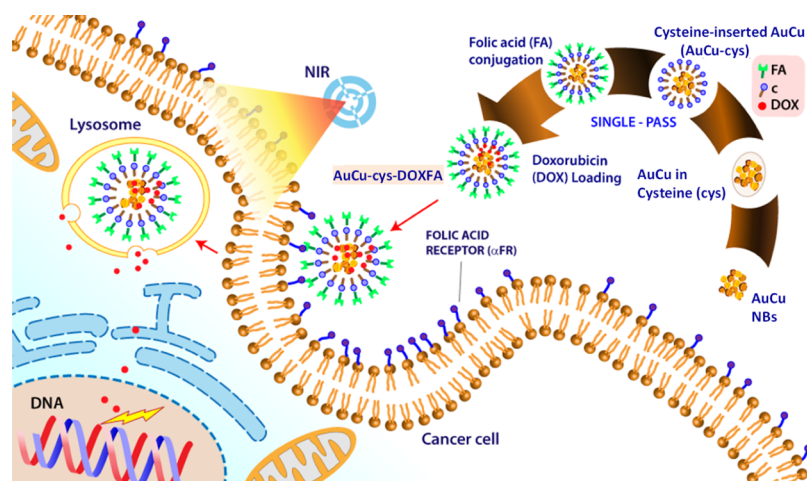


**Figure 1.** Schematic of the plug-and-play assembly route for the folate-receptor-targeted chemo-phototherapy, AuCu-cys-DOXFA. Electrically produced AuCu NBs were injected into cys solution and sprayed out as hybrid droplets. These droplets were directly exposed to 185 nm UV (6.2 eV photon energy vs Au [5.1 eV work function] and Cu [4.7 eV work function]) to initiate electrostatic attraction between photoionized AuCu (positively charged) and negatively charged groups ( $\text{SH}^-$ ) of cys to form AuCu-cys platforms in single-pass gas stream. The collected platforms were conjugated with FA and then stirred in DOX solution to load DOX for the formation of AuCu-cys-DOXFA.

duced, in which the system was designed and constructed with controllable reaction devices to respond to sudden changes in demand or ingredients.<sup>11</sup> However, addition of reactions to the digitizable process that facilitates the preparation of inorganic NPs has not yet been attempted. Moreover, using bimetallic NSs to produce composite pharmaceuticals may be a more complex process, and constructing a realizable system for such composites will be a significant challenge for future theranostics. Recent reports on using electrical discharges in gas streams have shown that they hold the potential to produce bimetallic NSs with high purity by modulation of the electric energy and discharge repetition rate.<sup>12,13</sup> Likewise, thermodynamic formation under a temperature gradient<sup>14,15</sup> with nucleation–condensation of copolymerized metals from electrical discharges in inert gas flows between different metal rods can induce the formation of bimetallic NSs. Even though electrical on–off controls for NS production can be produced, there are currently no relevant reports of their use for biomedical applications. AuCu nanobimetallics may be feasible components of optostimulus systems owing to the advantageous plasmonic properties of Au and Cu (light absorption in the longer wavelength region). Furthermore, the low cost and easy accessibility of Cu compared with other noble metals makes it an attractive candidate for realization in advanced therapeutics.<sup>16</sup> However, because of the inert nature of noble-metal NSs under physiological conditions, on-demand surface functionalization (in a continuous production configuration) is still required to produce conjugatable platforms that can be loaded with targeting, probing, protective, and/or therapeutic agents for practical bioapplications.

In this regard, the present study has attempted to develop a plug-and-play route to continuously producing conjugatable bimetallic AuCu platforms in which a continuous gas flow assembly system was designed and constructed in serial connection with three digitally operable devices (i.e., electrical, mechanical, and photonic). This requires only pushing the power button of the devices to yield conjugatable optostimulus platforms in a single-pass configuration as a built-to-order nanomedicine.<sup>17</sup> The resulting materials were employed as platforms to determine feasibilities in conjugation, loading, and

photothermal activity for cancer treatment (Figure 1). Specifically (Figure S1A), an electrical discharge (kV–mA mode for a single-discharge channel) between Au and Cu rods generated bimetallic vapors, and the vapors were immediately condensed into solid AuCu nanobunches (NBs) by nitrogen gas flow at room temperature. The digitally controlled, NB-laden flow was connected to a mechanical spraying device containing cysteine (cys) solution, and the NBs were sprayed out with cys solution as hybrid droplets (AuCu into cys droplets). The droplets entered a photonic device, still in the single-pass gas stream and were dynamically exposed to 6.2 eV photons, resulting in the formation of cys incorporated AuCu (the AuCu-cys platform) via electrostatic attraction between the photoionized (i.e., positively charged) AuCu and negatively charged thiol groups of cys. In this system, the cys would act as a bifunctional linker for other molecules by virtue of its thiol and amine groups.<sup>18,19</sup> By employing bimetallic AuCu configuration, the photoionization rate and saturation positive charges can be enhanced compared with monometallic Au (Figure S1B; Cu-4.7 eV vs Au-5.1 eV), implying that AuCu is more suitable for the electrostatic attraction to form AuCu-cys. The positive charges on AuCu NBs for electrostatic conjugation with cys molecules were confirmed by measuring particle charge current before and after photoionization (inset table of Figure S1B), supporting electron detachment from NBs to generate positive charges. After passing through an activated carbon-packed hollow tube, the platforms were subsequently collected on a substrate in powder form. The platforms were dispersed in deionized water or doxorubicin (DOX)-dissolved deionized water without any further purification. This dispersion was then added to folic acid (FA) to form AuCu-cys-FA or AuCu-cys-DOXFA because FA (endogenous ligand) can bind to human alpha folate receptor (FR) with high affinity ( $K_d$  up to 20 nmol L<sup>-1</sup>) and undergo internalization via receptor-mediated endocytosis.<sup>20,21</sup> Proliferating cancer cells (e.g., breast, ovarian, cervical, and colorectal) overexpress the FR because of elevated demand of folate when compared with normal cells,<sup>22</sup> implying that FA conjugation is a good option for targeting cancer therapeutics. DOX is a potent medication for the treatment of different

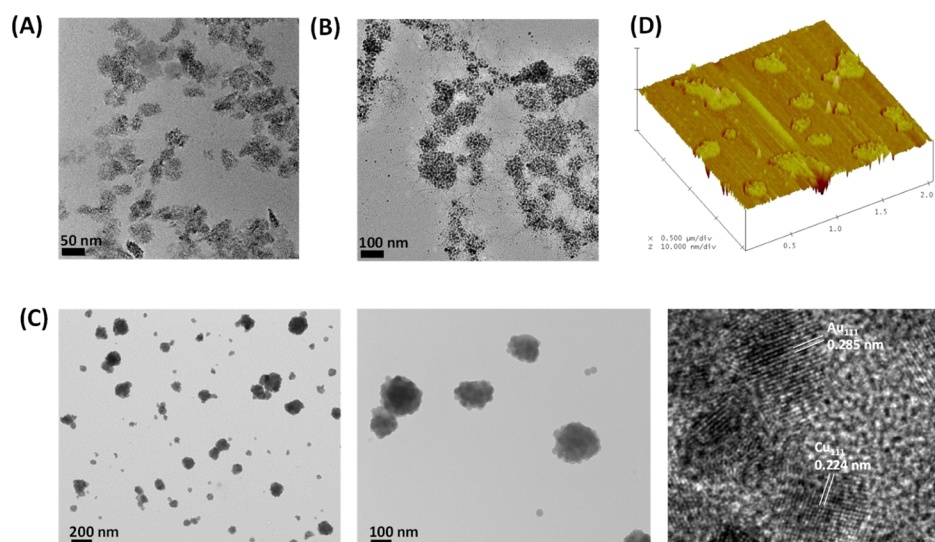


**Figure 2.** Morphological changes through direct cysteine insertion into AuCu NBs and subsequent FA conjugation. (A–C) TEM images of AuCu, AuCu-cys, and AuCu-cys-FA. The shape and contrast of AuCu were altered upon photoinduced cysteine insertion, and these were transformed further after FA conjugation. (D) 3D AFM topography of AuCu-cys-FA. This image exhibits platelets consisting of dots with thin layers, and the dots and layers matched AuCu-cys and FA, respectively. The lateral dimensions measured by AFM are consistent with the TEM image of AuCu-cys-FA.

hematologic and solid cancers,<sup>23</sup> and an extensive chemotherapeutic effect might be obtained by combining DOX with such targeted platforms. The resulting AuCu-cys-FA and AuCu-cys-DOXFA were finally used in both in vitro (MDA-MB-231 [FR overexpressing], MCF-7 [mildly FR expressing], and A549 cells [FR negative]) and in vivo (MDA-MB-231 xenograft bearing BALB/c nude mice) models to assess the efficacy of targeting and chemo-phototherapeutic activities. Dispersion stability, photothermal activity, biocompatibility, and pH- and photo-responsive DOX release properties, including physicochemical material characterizations, were also investigated to support the bioassays.

## RESULTS AND DISCUSSION

Size distributions of the AuCu NBs from an electrical discharge device and AuCu-cys from a mechanical spray device (Figure S2A and Table S1) were measured using a scanning mobility particle sizer (SMPS, 3936, TSI Inc., USA). Even though two different rods (Au and Cu) were used in the discharge, the products exhibited a unimodal nanosized distribution similar to those from a homogeneous Au or Cu discharge, demonstrating that the heterogeneous discharge produced well-combined AuCu nanobimetallics. The resulting AuCu was incorporated with cysteine solution to form hybrid droplets at the nozzle of a mechanical spray device via gas pressurization<sup>24</sup> and subsequently exposed to 6.2 eV photons in a photonic device to produce AuCu-cys still in a single-pass gas stream. The size distribution of AuCu-cys in the gas stream was also measured using the SMPS, and the results also revealed a unimodal distribution, suggesting that the cysteine molecules had coated the AuCu evenly. These characteristics were further confirmed via dynamic light scattering (DLS; Nano ZS, Malvern Instruments, UK) analyses on AuCu or AuCu-cys dispersed in phosphate-buffered saline (PBS; Figure S2B). The results also exhibited unimodal size distributions, although there were differences in the mean size because of the significantly higher concentrations (from long-term sampling to prepare dispersion unlike SMPS measurement [direct measurement in gas-phase]) of AuCu and AuCu-cys (inducing multiple scattering) used

during DLS measurement,<sup>25</sup> which implies that incorporation between the AuCu (or Au) and cysteine (or Cu) was robust enough (did not exhibit multimodal size distributions from segregation of AuCu NBs) even in the aqueous phase to maintain the heterogeneous structures. The significant difference in size distribution between the AuCu and AuCu-cys was due to inclusion of several AuCu NBs in a cysteine droplet during the assembly that causes a significant change in the distribution as bigger size-smaller concentration manner (refer to Figure S2A). In addition, the surface charges of AuCu and AuCu-cys were found to be  $-7.3$  and  $-16.4$  mV, respectively. The more negative value of AuCu-cys may be due to the zwitterionic properties of cysteine.<sup>26</sup> To determine whether there was a change in light absorption spectrum (Figure S2C) after the photoreaction of AuCu, UV-vis spectroscopy (T60, PG Instruments, UK) was performed on AuCu or AuCu-cys after dispersion in PBS (insets of Figure S2C). The plasmonic coupling from the bimetallic configuration clearly induced a broader near-infrared (NIR) absorption window than those from individual Au and Cu. The characteristic band of AuCu at around 550 nm remained as broadened after the photoreaction (6.4 s reaction time), which may be due to binding between the positively charged Au (or Cu) and the cysteine molecules (negatively charged thiols) during the reaction that also induce broadening in the resonance spectrum of the AuCu via hybridized (cysteine insertion) interparticle (Au–Cu) coupling. Morphological evolutions were assessed via transmission electron microscopy (TEM; Tecnai G<sup>2</sup> F20 S-TWIN, FEI, USA) measurements (Figure 2). Nucleation–condensation of the co-vaporized Au and Cu produced primary Au and Cu particles, and these particles were successively agglomerated via Brownian thermal collision in the gas stream, resulting in the formation of AuCu NBs (Figure 2A). Photon irradiation in the presence of cysteine molecules then transformed the NBs into AuCu-cys agglomerates (Figure 2B), and FA conjugation by immersing the agglomerates in FA solution further transformed the NBs into AuCu-cys-FA platelets (Figure 2C). The platelet structure was also verified via atomic force microscopy (AFM; Nanoscope IIIa, Digital Instruments Co., USA), and

the AuCu dots were hardly visible in the platelet structures (Figure 2D), demonstrating that tight FA conjugation with AuCu-cys can be achieved (i.e., the surface amine groups of AuCu-cys were conjugatable with FA in the aqueous phase). The increases in size from cys insertion and subsequent FA conjugation matched the results from SMPS and DLS analyses. The high-magnification TEM image of AuCu NBs (Figure S2D) revealed individual crystalline structures of Au (*d*-spacing [0.234 nm] for Miller [111] face-centered cubic [fcc] Au plane) and Cu (*d*-spacing [0.210 nm] for [111] fcc Cu plane),<sup>27,28</sup> which demonstrated a bimetallic (not alloyed) character of AuCu NBs, probably because of their different thermodynamic properties (i.e., melting point). Interestingly, the high-magnification TEM image of AuCu-cys (Figure S2E) also mostly revealed two different crystallites, but their *d*-spacings (0.285 and 0.224 nm) were not consistent with fcc Au and Cu planes. These differences suggest that direct cys insertion into crystalline Au (or Cu) matrix can be achieved through the photoreaction, demonstrating the feasibility of the plug-and-play route for the assembly of conjugatable photo-responsive platforms.

The valence states of AuCu and AuCu-cys, including individual Au and Cu atoms, were also determined to confirm cys insertion into AuCu. Figure S3A shows Au 4f core signals of AuCu, which can be resolved into typical doublets at 84.3 and 87.7 eV binding energies, attributed to 4f<sub>7/2</sub> (bulk Au atoms) and Au 4f<sub>5/2</sub> (surface Au atoms) in zero-valent states, respectively. There was slight shifting of the peaks (84.1 eV for Au 4f<sub>7/2</sub> and 87.6 eV for Au 4f<sub>5/2</sub>), which may be because of electrical interaction with Cu in AuCu.<sup>29</sup> Upon AuCu reaction with cys by photon irradiation to form AuCu-cys, decreases in Au binding energy were significant (83.1 eV for 4f<sub>7/2</sub> and 86.9 eV for 4f<sub>5/2</sub>) and the band widths broadened. This implies that cys insertion into AuCu induced changes in valence state,<sup>30,31</sup> suggesting that the photo-reaction was able to directly hybridize AuCu in the single-pass gas stream. Analogous results were obtained with Cu 2p core signals after photo-reaction (Figure S3B), although individual Cu exhibited satellite peaks at around 943 and 962 eV (presence of Cu<sup>2+</sup>) because of its lower ionization potential (7.73 eV) compared with Au (9.23 eV). However, the AuCu signals did not exhibit the satellite band, which confirms that ionizing metal with electrical discharge is preferable for lower ionization potentials.<sup>32</sup> cys insertion and successive FA conjugation were examined by comparison with individual cys and FA using Fourier transform infrared spectroscopy (FTIR; iS-10, iS-10, Thermo Electron, USA; Figure S3C). The spectrum of cys exhibited a broad band at 2700–3300 cm<sup>-1</sup>, which can be assigned to the NH– stretching mode of amine groups, and a relatively small peak at around 2550 cm<sup>-1</sup> that can be assigned to S–H group. The magnitudes of these characteristic bands were significantly reduced in the spectrum of AuCu-cys with slight shifts in band positions, suggesting that direct cys insertion was achieved in the single-pass photo-reaction.<sup>33</sup> The spectrum of FA exhibited intense peaks at around 1600 cm<sup>-1</sup>, which can be attributed to the stretching vibrations of carbonyls from the amide and acidic groups of FA. Other peaks at around 1500 cm<sup>-1</sup> can be attributed to benzoic vibrations and aromatic ring stretching vibrations, respectively. Similarly, these major peaks exhibited positional shifts and intensity decreases in AuCu-cys-FA, further verifying that FA was loaded onto AuCu-cys.<sup>18</sup> FA conjugation was further confirmed by UV–vis spectra by comparison among AuCu-

cys, AuCu-cys-FA, and individual FA (Figure S4D). The characteristic absorption peak of FA at around 350 nm could be also detected in AuCu-cys-FA, while AuCu-cys produced a featureless spectrum, implying that FA was indeed conjugated with AuCu-cys.<sup>34</sup> Interestingly, the broadband absorption spectrum at wavelengths longer than 400 nm did not change significantly, suggesting that AuCu-cys-FA might be active both in utilizing FR for cellular targeting and in absorbing light for photothermal conversion.<sup>35,36</sup> The colloidal stability of AuCu-cys-FA was examined by monitoring UV–vis spectra upon dispersion in PBS (Figure S3E), and no significant changes were found for the entire testing period (one month). Unipolar surface charges on AuCu-cys-FA may induce this stability via repulsive forces, which also further indicates an effective conjugation of FA with AuCu-cys.

The photothermal activity of AuCu-FA was examined upon exposure to NIR laser irradiation (808 nm, 2.5 W cm<sup>-2</sup>, 5 min). AuCu-FA dispersions at concentrations of 0.10, 0.15, and 0.20 mg mL<sup>-1</sup> produced 4.04, 5.66, and 6.54 °C min<sup>-1</sup> temperature elevations, respectively (Figure S4A). Similarly, the 0.15 mg mL<sup>-1</sup> dispersion exhibited temperature elevation rates of 3.72, 5.66, and 6.58 °C min<sup>-1</sup> when exposed to NIR with increasing power densities of 1.8, 2.5, and 3.0 W cm<sup>-2</sup>, respectively (Figure S4B). It should be noted that repetitive irradiation of AuCu-cys-FA resulted in repeatable temperature elevation, although the magnitude of the elevation decreased slightly with each sequential 5 min exposure (Figure S4C). This suggests that AuCu-cys-FA retained photothermal capability even after repeated NIR exposure, unlike Au nanorods, which deform (melt) and lose NIR absorbance capability after repeated irradiation.<sup>37</sup> This photostability was further confirmed by recording UV–vis spectra after each exposure (Figure S4D). The absorbance at 808 nm did not decrease significantly after each repetitive exposure, but, interestingly, the band intensity between 400 and 800 nm decreased noticeably. These decreases in intensity might hint at solid-state diffusion of Cu into Au at increased photothermal temperatures to form ordered or disordered AuCu alloys or might hint at the formation of Cu<sub>2</sub>S through further reaction with cys.<sup>27,38–40</sup>

Thermogravimetric analysis (TGA; Diamond TG/DTA, PerkinElmer, USA) of AuCu-cys, AuCu-cys-FA, and AuCu-cys-DOXFA was conducted in the temperature range of 25–750 °C under nitrogen flow (Figure S5A). AuCu-cys-DOXFA exhibited a weight loss of 27.35% relative to AuCu-cys-FA, which correlates with the thermal decomposition of loaded DOX. TGA also provided information on the amount of conjugated FA, which was 6.77%. The spectrometric method was not used to determine the FA content as its fluorescence is known to be quenched by close proximity to plasmonic surfaces.<sup>28,41</sup> The loading capacity of DOX onto AuCu-cys-FA was further determined by solubilizing the DOX from a known quantity of freeze-dried AuCu-cys-DOXFA; this was found to be 21.9 ± 4.6% w/w (which is consistent with the value determined by TGA). This capacity may have been due to electrostatic binding of cationic DOX to the carboxylic groups of cys as well as to capillary suction from voids between the cys inserted primary Au and Cu particles.

The DOX release profile was investigated in PBS at pH 7.4 (which mimics physiological conditions) and in acetate-buffered saline at pH 5.5 (which mimics endolysosomal conditions; Figure S5B). AuCu-cys-DOXFA exhibited a *t*<sub>1/2</sub> (time required to release 50% content) of approximately 6 h at

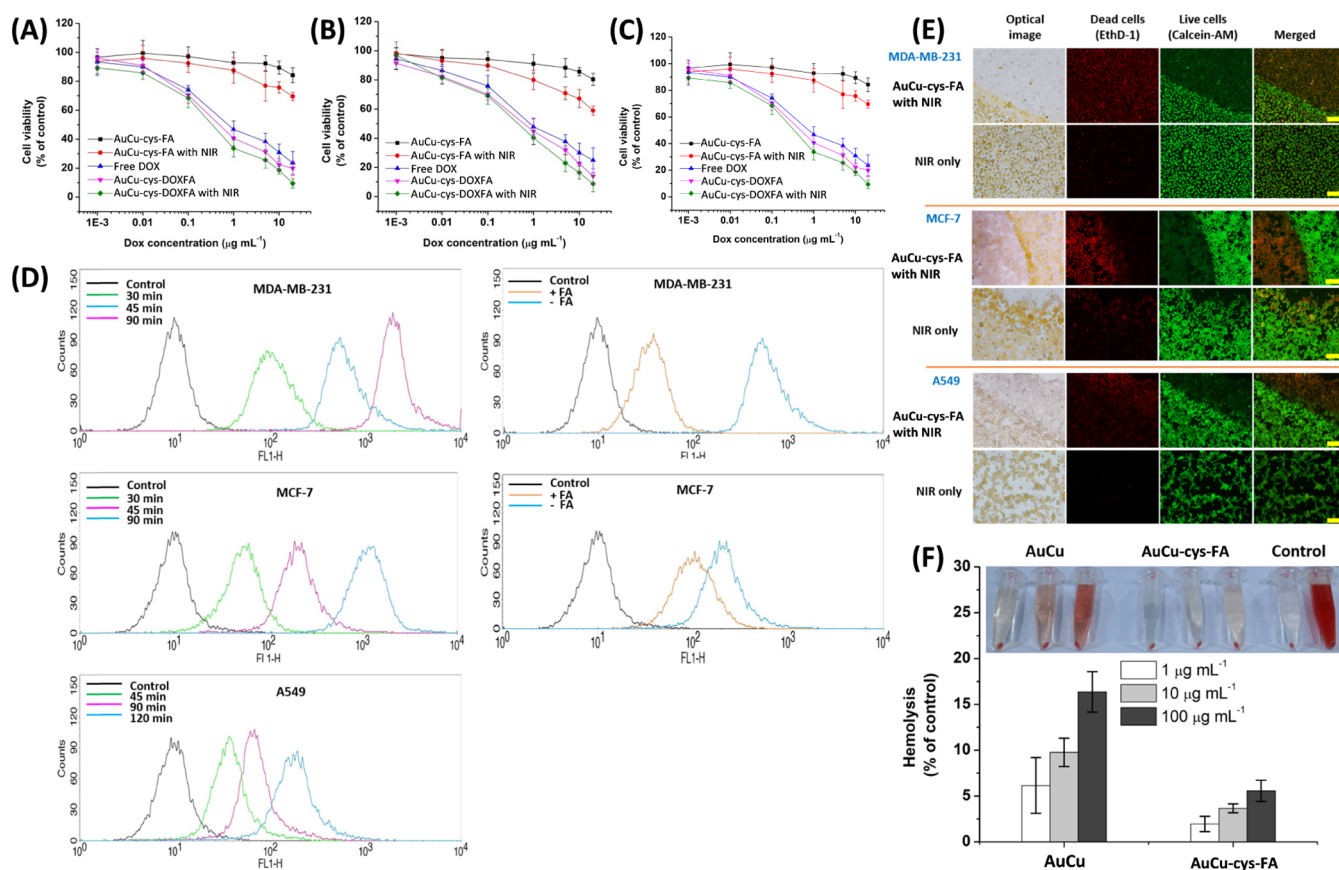


**Figure 3.** In vitro anticancer activities of AuCu-cys-FA and AuCu-cys-DOXFA with and without NIR irradiation ( $0.8 \text{ W cm}^{-2}$ , 150 s) in MDA-MB-231, MCF-7, and A549 cell lines, including hemolysis results. (A–C) Cytotoxicities from the different treatments analyzed via the MTT assay, compared with free DOX. (D) FACS measurements to determine cellular uptake of AuCu-cys-FA by the three cell lines. Competitive binding was demonstrated by pretreating cells with 5 mM FA prior to incubation with AuCu-cys-FA. (E) Live/Dead assay after NIR irradiation with and without AuCu-cys-FA (scale bars: 200  $\mu\text{m}$ ). (F) Hemolysis assay of AuCu and AuCu-cys-FA in an SD rat erythrocyte dispersion. Inset digital images show supernatants after incubation with AuCu and AuCu-cys-FA.

pH 5.5, while sustained release was observed at pH 7.4 with a  $t_{1/2}$  of approximately 18 h. The  $t_{1/2}$  values could be varied by modulating photoionization conditions (reaction time and UV intensity) that facilitate anchoring strength of DOX. The faster DOX release at pH 5.5 may be due to pH-dependent solubility and amphoteric nature of DOX ( $\text{pK}_a \approx 7.2\text{--}8.2$ ), where the amine groups of DOX underwent protonation and became more soluble. This pH-dependent release is desirable in cancer therapy because significantly less DOX will leach out during long-term circulation of AuCu-cys-DOXFA in the blood, while the low pH in tumor interstitia and in subcellular endolysosomal compartments will trigger accelerated DOX release and so produce a more effective chemotherapeutic effect.

The on-demand release of DOX from AuCu-cys-DOXFA triggered by NIR irradiation was further examined (Figure S5C). A dispersion of AuCu-cys-DOXFA was irradiated ( $2.5 \text{ W cm}^{-2}$ ) twice for 5 min with a 1 h interval. The first irradiation induced burst release of 21% of the DOX and the second induced the sudden release of another 25%. The total release after the two NIR exposures was 85% over 70 min, while only 26% was released over the same period in the absence of NIR irradiation. These pH- and photo-triggered release properties validated the feasibility of AuCu-cys-DOXFA for use as chemo-phototherapy.

To confirm colloidal stability of AuCu-cys-DOXFA, DLS size distributions of AuCu-cys-DOXFA dispersed in PBS were monitored for 30 days at ambient condition (Figure S6), and there were no significant shifts in size distribution of AuCu-cys-DOXFA during the monitoring. Even though the powder formulation of AuCu-cys-DOXFA after the assembly and direct collection was dispersed in buffered saline just before bioassays, stability of AuCu-cys-DOXFA could also be achieved even dispersed in buffered saline right after the assembly, implying that the plug-and-play assembly may be a workable protocol to stably produce functionalized inorganic nanostructures for advanced therapeutics. A disintegratable activity of AuCu-cys-DOXFA upon NIR irradiation was evaluated by TEM observation because the size decrease of inorganic-based nanomaterials into smaller ones through disassembly in the body is essential for the clinical translation with favorable clearance behaviors and minimal side effects.<sup>42</sup> The AuCu-cys-DOXFA was exposed to NIR laser ( $2.5 \text{ W cm}^{-2}$ , 5 min) thrice with 5 min interval, and morphologies upon NIR irradiations (0–3 times) were observed (Figure S7A–D). The disintegration of AuCu-cys-DOXFA upon the irradiations might be due to partial release and/or degradation of cys-DOXFA components from NIR-induced heat generation (melts or deforms the structure)<sup>43</sup> that causes fragmentation into smaller pieces. The decreases in cys and FA absorbance in FTIR analysis (Figure S7E) supported the

fragmentation after NIR irradiation. This further suggests that nanostructures based on NBs (consisted of ultrafine [ $<10$  nm] nanoparticles like AuCu-cys-DOXFA) may be a safer platform for advanced therapeutics.

Cytotoxicities of AuCu-cys-FA, AuCu-cys-DOXFA, and free DOX were evaluated using the 3-(4,5-dimethylthiazol-2-yl)-2,5-diphenyltetrazolium bromide (MTT) assay in MDA-MB-231, MCF-7, and A549 cell lines after 48 h of incubation (Figure 3A–C). AuCu-cys-FA produced  $>80\%$  viability in all cell lines at the tested concentrations, demonstrating applicability of AuCu-cys-FA for systemic administration. This may be attributable to cysteine insertion into AuCu and subsequent FA conjugation. DOX exhibited dose-dependent cytotoxicity in all cell lines with an  $IC_{50}$  of  $1 \mu\text{g mL}^{-1}$ . The  $IC_{50}$  values decreased by half when cells were incubated with AuCu-cys-DOXFA containing equivalent amounts of DOX (Table S2). This suggests that FA conjugation, and the resultant transmembrane delivery of payload, increased the efficiency of intracellular DOX delivery. Encapsulated DOX could thus escape cellular efflux via transmembrane P-glycoprotein pumps, which can be overexpressed in drug-resistant cells. Nevertheless, the 48 h incubation (i.e., providing sufficient time) induced similar cytotoxicities in all three (FR over-expressing, mildly FR expressing, and FR negative) cell lines, which might be due to subcellular entry via nonspecific endocytic routes during the incubation, as discussed in previous reports.<sup>44–47</sup> This suggests that the folate receptor-mediated endocytosis might be a significant parameter for cellular internalization of circulating AuCu-cys-DOXFA in vivo conditions. The effect of NIR exposure following AuCu-cys-FA and AuCu-cys-DOXFA incubation was also evaluated to determine chemo-photothermal activity. All cell lines incubated with AuCu-cys-FA and irradiated with NIR ( $0.8 \text{ W cm}^{-2}$ ) exhibited 40–50% cell death at  $20 \mu\text{g mL}^{-1}$ , suggesting that photothermal killing was effective in all cell types. This was further enhanced by the presence of DOX because the cells were exposed to burst-released DOX from AuCu-cys-DOXFA upon NIR irradiation.

The cellular uptake of fluorescein isothiocyanate (FITC)-loaded AuCu-cys-FA was monitored by fluorescence-activated cell sorting (FACS; BD FACS Verse, BD Biosciences, USA) analysis in the three cell lines. FR is known to be highly expressed in MDA-MB-231, moderately expressed in MCF-7, and unexpressed in A549 cells (Figure 3D).<sup>20,48</sup> All cell lines exhibited time-dependent cellular uptake of FITC-loaded AuCu-cys-FA, but the FR-expressing cells exhibited higher fluorescence shifts (MDA-MB-231  $>$  MCF-7) at identical incubation times than nonexpressing cells (A549), suggesting that FR-mediated endocytosis was a significant uptake mechanism. This suggests that targeting of FR-overexpressing cancers can be achieved by FA conjugation to AuCu-cys.

To further validate the targeting mechanism of AuCu-cys-FA, a competitive binding experiment was conducted. MDA-MB-231 and MCF-7 cells were pretreated with excess of FA for 1 h to completely block the FR prior to 45 min incubation with FITC-loaded AuCu-cys-FA. Fluorescence intensity decreased significantly, indicating a reduced uptake of AuCu-cys-FA as a result of prior FR saturation. This finding was further confirmed by intracellular localization studies using confocal microscopy (A1Si, Nikon, Japan; Figure S8A). Upon incubation of MDA-MB-231 cells with FITC-loaded AuCu-cys-FA (green fluorescence) and co-staining with LysoTracker Red (red fluorescence for lyso/endosomes), high intensity

green fluorescence could be observed that overlapped with red fluorescence, suggesting enhanced FR-mediated endosomal internalization of AuCu-cys-FA. In contrast, the cells pretreated with FA produced relatively weak green fluorescence signals from AuCu-cys-FA with nonuniform colocalization with red fluorescence. A similar trend was observed with FA-pretreated MCF-7 or FR-negative A549 cells, verifying that FA-conjugated AuCu-cys-FA can selectively bind to and be internalized by FR-expressing cancer cells. It should be noted that both FACS and confocal microscopy analyses revealed cellular uptake of AuCu-cys-FA into both FR-expressing and FR-negative cells, which confirms that nonspecific endocytosis is also involved in intracellular uptake of AuCu-cys-FA.

The phototherapeutic performance of AuCu-cys-FA was investigated in the same three cell lines by a live/dead assay (Figure 3E). When the NIR laser light ( $2.5 \text{ W cm}^{-2}$ , 5 min) was focused on a cell monolayer incubated with AuCu-cys-FA, circular regions of dead cells (stained red with ethidium homodimer [EthD]-1) were visualized for all the cell lines. A distinct boundary between the beam spot and live cells (stained green with Calcein-AM) demonstrated that cell death occurred in irradiated regions only, while no marked cell destruction was after irradiation of untreated cells. This suggests that phototherapy using AuCu-cys-FA can be highly localized to superficial solid tumors without harming adjacent healthy tissues.

The cytotoxic mechanism of AuCu-cys-DOXFA was investigated by determining the level of cellular apoptosis in the three cell lines (Figure S8B). In all cell lines, DOX increased the early-apoptotic (EA) and late-apoptotic (LA) cell population. Cells incubated with AuCu-cys-DOXFA and irradiated with NIR laser light exhibited even more apoptosis in the order of MDA-MB-231 (34.87% LA, 49.21% EA)  $>$  MCF-7 (21.32% LA, 41.25% EA)  $>$  A549 (8.51% LA, 28.63% EA), which correlated with FR expression levels. This implies that the FR-mediated cellular uptake of AuCu-cys-DOXFA plays a key role in high payload DOX delivery and consequent enhancement of DOX-induced apoptosis. It is important to note that NIR irradiation alone provoked only slight necrosis ( $<3\%$ ), as shown in the upper left quadrant that indicates a necrotic cell population. This was further confirmed by a western blot assay for the pro-apoptotic marker, p53 (Figure S8C). DOX induces DNA damage by inhibiting topoisomerase II and activates several molecular pathways to apoptosis depending on dose and cell types, which are accompanied by upregulation of the multifunctional transcription factor p53.<sup>49,50</sup> DOX and AuCu-cys-DOXFA increased p53 level compared with the untreated controls in MCF-7 and A549 cells, suggesting a p53-dependent anticancer mechanism. However, MDA-MB-231 cells possess a mutated p53 gene that is functionally inactive,<sup>51</sup> and, therefore, expression of the pro-apoptotic marker BAX was instead examined in these cells. Upon laser irradiation, the cells incubated with AuCu-cys-FA also exhibited increased p53 or BAX band intensities compared with the control. This verified that phototherapy can be used to modulate apoptotic ablation of cancer cells. Aside from induction of apoptosis, DNA damage by the cytostatic drug, DOX, also causes cell cycle arrest in cancer cells. Cell cycle analysis of the three cell lines after treatment with AuCu-cys-DOXFA was performed using a redox dye (Figure S9). In MDA-MB-231 cells, DOX primarily arrested the cell cycle in the G1 phase. MCF-7 cells incubated with DOX exhibited a major fraction in G1 phase and a minor fraction in G2M phase,

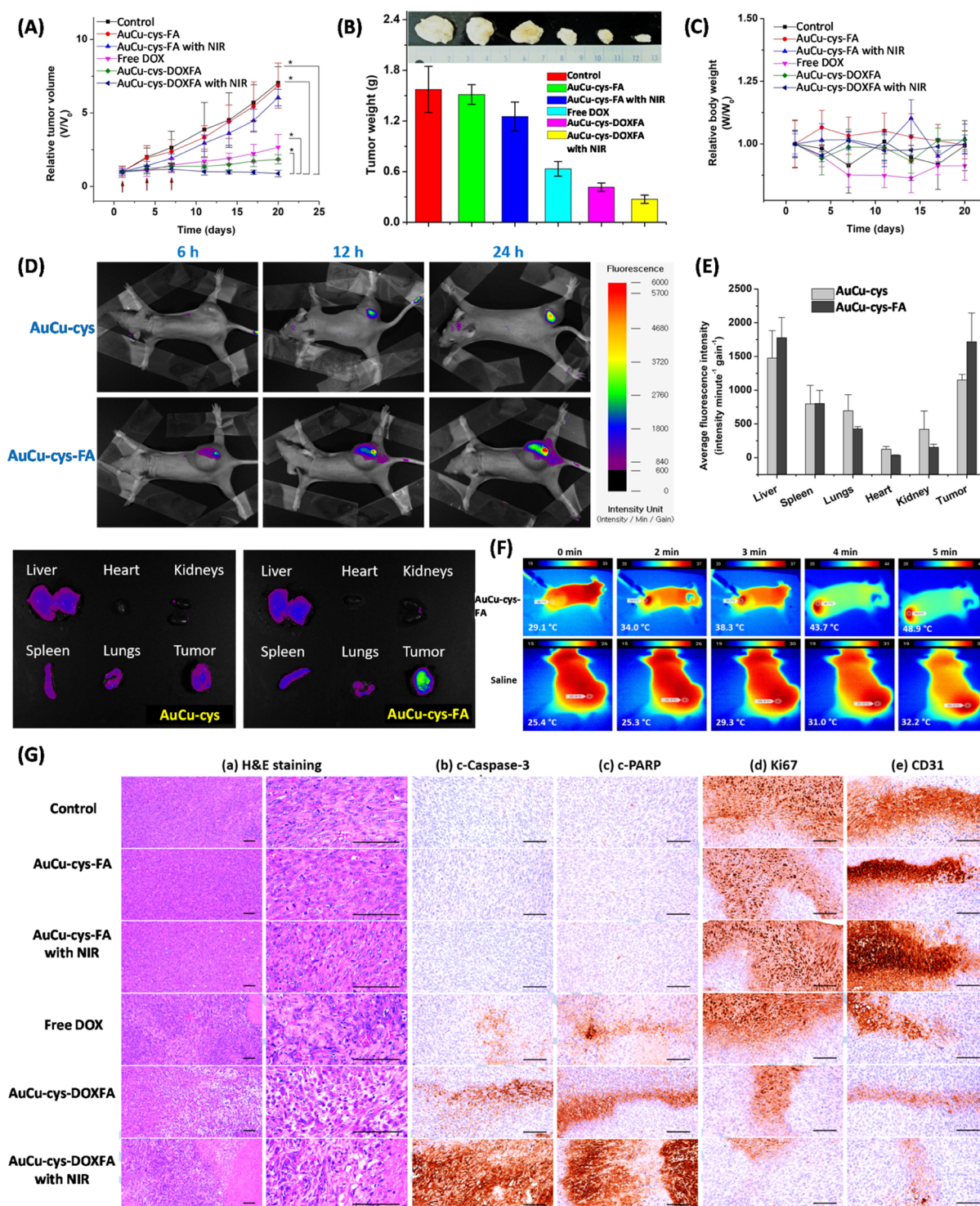


**Figure 4.** In vivo antitumor activities of AuCu-cys and AuCu-cys-FA, including AuCu-cys-DOXFA. (A) 20 d monitoring of relative tumor volumes in mice groups undergoing different treatments ( $N = 5-6$ ). The arrows represent the days (0, 3, and 6) of intravenous injection. The NIR groups received laser (808 nm,  $2.5 \text{ W cm}^{-2}$ ) for 3 min 12 h postinjection. (B) Average weights of excised tumors from the different groups ( $N = 3$ ). The inset digital image shows tumors excised from the different groups. (C) 20 d monitoring of relative mice body weights during the different treatments. (D) In vivo biodistributions in MDA-MB-231 xenograft bearing nude BALB/c mice (upper panel) and ex vivo fluorescence distributions in major organs and tumors (lower panel) after intravenous administration of Cy5.5-conjugated AuCu-cys and AuCu-cys-FA. (E) Corresponding average fluorescence intensities of major organs and tumors ( $N = 3$ ). (F) In vivo photothermal images after NIR laser irradiation (5 min) of tumors from PBS and AuCu-cys-FA administered mice. (G) H&E and immunocytochemically stained tumor sections from the different treatment groups, including staining for c-Caspase-3, c-PARP, Ki67, and CD31 (scale bars: 120  $\mu\text{m}$ ).

whereas DOX treated A549 cells exhibited a significantly higher subpopulation of cells at the G1 check point. DOX arrested cell cycle in different phases might be due to diverse

expressions of the cells from different genetic aberrations, as introduced in a previous report.<sup>52</sup> In all cells, this trend was exaggerated by treatment with AuCu-cys-DOXFA, which

facilitates enhanced cellular internalization of DOX. On the other hand, MCF-7 cells treated with AuCu-cys-DOXFA containing an equivalent DOX concentration exhibited a markedly high level of cells in G2M compared with G1 phase, which correlates with the degrees of FR expression. Considering the likelihood of intravenous administration of AuCu-cys-DOXFA, its interaction with red blood cells (RBCs) was evaluated using a hemolytic assay (Figure 3F). Untreated AuCu NBs at a high concentration ( $100 \mu\text{g mL}^{-1}$ ) induced about 16% membrane lysis in RBCs, while AuCu-cys-FA produced significantly reduced membrane damage and lysis (<5%) at the same concentration, suggesting enhanced hemocompatibility of AuCu-cys-FA compared with uncoated AuCu NBs. Intracellular reactive oxygen species (ROS) generation of AuCu-cys and AuCu-cys-DOXFA with NIR irradiation was also investigated. The green fluorescence (representing ROS generation) of 2',7'-dichlorofluorescein could be clearly seen in AuCu-cys-treated cells under NIR irradiation (Figure S10A). The ROS generation from this treatment configuration was greater than that from free DOX treatment (Figure S10B), suggesting photosensitizing capacity of AuCu-cys for effective photothermal therapy. This property thus induced a desirable synergistic activity in ROS generation (particularly in MDA-MB-231 and MCF-7 cells) after DOXFA conjugation with AuCu-cys.

In vivo antitumor efficacies of AuCu-cys-FA and AuCu-cys-DOXFA with or without NIR irradiation 24 h post-injection were evaluated in FR-expressing MDA-MB-231 xenograft-bearing BALB/c nude mice. The changes in relative tumor volume as a function of time following intravenous injection are shown in Figure 4A. The untreated control group exhibited a rapid increase in the tumor volume. Even though the NIR-irradiated AuCu-cys-FA group exhibited a reduction of tumor volume (14.2%), there were no significant differences between DOX-free groups (control, AuCu-cys-FA, and AuCu-cys-FA with NIR groups). In contrast, by the end of the experimental period (20 days), the DOX-loaded groups (DOX, AuCu-cys-DOXFA, and AuCu-cys-DOXFA with NIR) exhibited reductions of 62.2, 73.9, and 87.5%, respectively. Thus, DOX-loaded AuCu-cys-FA was highly efficacious at tumor regression compared with free DOX because of its targeting ability, and this was further enhanced upon NIR irradiation due to triggered DOX burst release. Figure 4B shows the average tumor weights from three randomly selected mice from each group, and the results are consistent with tumor volume monitoring. As an indicator of systemic toxicity, the relative body weights of mice from each group were determined and the change profiles were plotted (Figure 4C). The free DOX group exhibited about a 15% weight loss on most days, which finally stabilized to >8%, while the other groups did not exhibit significant weight loss.

In vivo biodistribution imaging of Cy5.5-conjugated AuCu-cys and AuCu-cys-FA was performed in subcutaneous MDA-MB-231 xenografted tumor-bearing mice following intravenous injection (Figure 4D). The top panel exhibits fluorescence signals of Cy5.5-conjugated AuCu-cys and AuCu-cys-FA in live mice at 6, 12, and 24 h post-injection. In AuCu-cys-FA injected mice, Cy5.5 signal was readily apparent in the tumor nodes at 6 h, while no signal was detected in AuCu-cys-injected mice. This suggests that the FR-homing ability of FA ligands resulted in earlier localization of AuCu-cys-FA to the FR-rich tumor site. As AuCu-cys and AuCu-cys-FA progressively accumulated in the tumor, the signal intensities in both mice gradually

increased and were clearly discernible at 12 and 24 h, respectively. AuCu-cys-FA-injected mice exhibited a significantly higher fluorescence signal intensity over the entire tumor node with a clear boundary between adjacent nontumor tissues at 24 h postinjection. In contrast, AuCu-cys-injected mice exhibited a relatively smaller area with a weaker fluorescence signal intensity. Nevertheless, both AuCu-cys and AuCu-cys-FA were compatible with long-term circulation following intravenous administration. In particular, the appearance of concentrated fluorescence signals at tumor sites in AuCu-cys-injected mice suggests that nonspecific and passive tumor perfusion may have occurred via a mechanism called the enhanced permeation and retention effect, in which nanosized particles can enter the interstitia of tumors through leaky microvasculature.<sup>53–55</sup> After 24 h, the mice were sacrificed by CO<sub>2</sub> asphyxiation, and major organs and primary tumors were isolated for ex vivo imaging (Figure 4D, lower panels). Both AuCu-cys and AuCu-cys-FA were identified in the liver, lungs, kidneys, and spleen. Signals were imperceptible in the heart, which is clinically favorable for DOX delivery because DOX is known to be highly cardiotoxic.<sup>56</sup> The fluorescence signals in the major organs and tumor nodules ( $N = 3$ ) were quantified (Figure 4E). Even though there were no significant differences in fluorescence intensity between AuCu-cys and AuCu-cys-FA in the major organs, AuCu-cys-FA exhibited a significantly greater fluorescence intensity in tumors than did AuCu-cys. This indicates that the FA ligand did not influence nonspecific binding to FR-negative normal tissues. Although FR has also been found in normal tissues and epithelia, it is relatively inaccessible to circulating AuCu-cys-FA because of its localization to apical epithelia.<sup>57,58</sup>

To provide additional evidence of feasibility in phototherapy, in vivo photothermal temperature elevation was investigated in subcutaneous MDA-MB-231 xenografted tumor (approximately 2000 mm<sup>3</sup>)-bearing mice upon AuCu-cys-FA or PBS (as control) injection via the tail vein (Figure 4F). After 24 h, the mice were restrained, and tumor nodule was illuminated with a NIR laser. Real-time thermal images were recorded with a thermal camera (Therm-App TH, Opgal Optronic Industries Ltd., Israel). The local surface temperature of the AuCu-cys-FA-treated tumor linearly increased to 48.9 °C from ambient temperature (29.1 °C) within 5 min under NIR irradiation, while for control mice it exhibited only a slight increase from 25.4 to 32.2 °C.

Ex vivo histological analyses of tumor sections from mice from the antitumor studies were performed using hematoxylin and eosin (H&E) staining (Figure 4G). Compared with control, AuCu-cys-DOXFA-treated mice exhibited a significantly reduced tumor cell volume along with other microstructural alterations, such as apoptotic condensations and necrosis. *In situ* immunohistochemical assays revealed brown staining corresponding to the expression of c (cleaved)-Caspase-3, c-poly(ADP-ribose) polymerase (PARP), Ki67, and CD31 (platelet endothelial cell molecule 1 [PECAM-1]) proteins in the tumor microsections. The apoptotic markers c-Caspase-3 and c-PARP increased, whereas Ki67 and CD31, which are proliferation and angiogenic markers, respectively, decreased significantly in the tumor samples from the AuCu-cys-DOXFA irradiated group compared with the control and other treated groups. The summarized data for the histological and immunohistochemical analyses are presented in Table S3. The effects of AuCu-cys-DOXFA in the absence and presence of NIR irradiation, including AuCu-cys and free DOX for

comparison purposes were further analyzed via histopathological observation of H&E-stained microsections of major organs (Figure S11). No significant histopathological findings (lesions, atrophy, and cellular fragmentation or swelling) were observed in AuCu-cys-DOXFA and AuCu-cys treatment groups compared with control and free DOX groups, suggesting effective loading, minimum premature, and off-site release of DOX in spite of existence of AuCu-cys and AuCu-cys-FA in the major organs.

## CONCLUSIONS

A plug-and-play route (serial connection of electrical, mechanical, and optical devices) to continuously assemble AuCu-cys for use as biocompatible, conjugatable and photostimulatable platforms was demonstrated, and these platforms exhibited a significant FR-targeted chemo-phototherapeutic activity. The platforms could be functionalized by adding a dispersion to an FA (and then DOX) solution. FA conjugation with AuCu-cys (i.e., AuCu-cys-FA) was effective in targeting FR rich cancer, as well as improving biocompatibility; thus, efficient selective uptake could be produced via FR-mediated endocytosis. DOX loaded onto AuCu-cys-FA (i.e., AuCu-cys-DOXFA) produced significant tumor regression in vivo via a synergistic effect of photo-induced hyperthermia, ROS generation, and DOX burst release upon NIR irradiation. These findings, stemming from the plug-and-play assembly of conjugatable and photostimulatable platforms, may not only offer a realizable concept for on-demand cancer nanomedicines, but also provide significant insights into the digitization of future pharmaceuticals.

## METHODS

The plug-and-play system to produce first AuCu-cys platforms consisted of three major parts, electrical discharge reactor, mechanical spray device, and photoirradiation tube, and was directly connected in a single-pass gas flow (Figure S1). A high temperature channel (~1 mm diameter, ~5500 °C) from the discharge between Au (3 mm diameter, AU-172561, Nilaco, Japan) and Cu (3 mm diameter, CU-112564, Nilaco, Japan) rods inside the reactor (27 cm<sup>3</sup> volume) produce AuCu NBs via evaporation, condensation, and agglomeration that were carried by nitrogen gas flow (1.57 L min<sup>-1</sup>, controlled by a digital flow meter [Kojima Instruments, Japan]). This AuCu-laden flow was employed as the operating gas for the spray device containing cys solution (0.1 mg mL<sup>-1</sup>). The NBs were injected into cys solution via gas pressurization near the nozzle in the device, and sprayed out as hybrid (AuCu NBs containing cys) droplets. These droplets were then directly exposed to 185 nm UV for 6.4 s at 47 °C gas temperature to insert cys into AuCu and extract solvent simultaneously. The electron detachment from the NBs via photoionization induced electrostatic attraction between the positively charged AuCu and negatively charged groups (SH<sup>-</sup>) of cys, resulting in the formation of AuCu-cys platforms. The platforms were separated from the gas flow through electrostatic precipitation on a polished aluminum rod as powder form.

The platforms were first dispersed in deionized water to be added to FA solution. To prepare the FA solution, 4.5 mg of FA was dissolved in 5 mL of dimethyl sulfoxide under sonication. To activate carboxylic groups of FA, 1.2 times the moles of 1-ethyl-3-(3-dimethylaminopropyl)carbodiimide (EDC; Tokyo Chemical Industry, Japan) and *N*-hydroxysuccinimide (NHS; Tokyo Chemical Industry, Japan) were further added and stirred for 2 h at room temperature. The previously prepared AuCu-cys platform dispersion was finally added into the FA solution, followed by stirring for 3 h. The EDC and NHS left the carboxylic groups upon FA was conjugated with amine groups on the platform that causes the surface charge of AuCu-cys-FA negative for its electrostatic binding with

DOX. The reacted platforms with FA (i.e., AuCu-cys-FA) were collected by centrifugation and washed thrice with PBS, and the dispersion was stored at 4 °C for characterizations and bioassays. To prepare DOX containing AuCu-cys-FA (i.e., AuCu-cys-DOXFA), in addition, the platforms were dispersed in DOX-dissolved deionized water and stirred overnight for DOX loading, and the dispersion was stored at 4 °C until further studies.

## ASSOCIATED CONTENT

### Supporting Information

The Supporting Information is available free of charge on the ACS Publications website at DOI: 10.1021/acsami.9b02330.

Experimental details; preparation diagrams of AuCu-cys, AuCu-cys-FA, and AuCu-cys-DOXFA; theoretical photoionization rate, saturation charge, and aerosol charge current of Au and AuCu; SMPS and DLS size distributions, UV-vis and XPS spectra, and low- and high-magnification TEM images of AuCu and AuCu-cys; spectral comparison between AuCu-cys and AuCu-cys-FA; dispersion stability results of AuCu-cys-FA; photothermal activity of AuCu-cys-FA; thermogravimetric analyses of AuCu-cys, AuCu-cys-FA, and AuCu-cys-DOXFA; pH-dependent and NIR-triggered D release of AuCu-cys-DOXFA; dispersion stability of AuCu-cys-DOXFA for 30 days; TEM images and FTIR spectra of AuCu-cys-DOXFA upon laser irradiation (1st–3rd); cellular uptake, western blot, and cell cycle analyses of AuCu-cys-FA and AuCu-cys-DOXFA; intracellular ROS generation; histopathological analyses for major organs; and summaries of size distributions, IC<sub>50</sub> values, and histomorphometrical analyses (PDF)

## AUTHOR INFORMATION

### Corresponding Authors

\*E-mail: hwangjh@yonsei.ac.kr (J.H.).

\*E-mail: jongohkim@yu.ac.kr (J.O.K.).

\*E-mail: postjb@yu.ac.kr (J.H.B.).

### ORCID

Jong Oh Kim: 0000-0002-4929-851X

Jeong Hoon Byeon: 0000-0003-0903-7128

### Notes

The authors declare no competing financial interest.

## ACKNOWLEDGMENTS

This research was supported by Basic Science Research Program through the National Research Foundation of Korea (NRF) funded by the Ministry of Science, ICT and future Planning (2018R1A2A1A05020683). This research was also supported by the NRF (2018R1A2A2A05021143) grant funded by the Korean Government and the Medical Research Center Program (2015R1A5A2009124) through the NRF funded by MSIP.

## REFERENCES

- (1) Huang, Y.; Xiao, Q.; Hu, H.; Zhang, K.; Feng, Y.; Li, F.; Wang, J.; Ding, X.; Jiang, J.; Li, Y.; Shi, L.; Lin, H. 915 nm Light-Triggered Photodynamic Therapy and MR/CT Dual-Modal Imaging of Tumor Based on the Nonstoichiometric Na<sub>0.52</sub>YbF<sub>3.52</sub>:Er Upconversion Nanoprobes. *Small* **2016**, *12*, 4200–4210.
- (2) Baek, S.-W.; Park, G.; Noh, J.; Cho, C.; Lee, C.-H.; Seo, M.-K.; Song, H.; Lee, J.-Y. Au@Ag Core-Shell Nanocubes for Efficient Plasmonic Light Scattering Effect in Low Bandgap Organic Solar Cells. *ACS Nano* **2014**, *8*, 3302–3312.

- (3) Rioux, D.; Meunier, M. Seeded Growth Synthesis of Composition and Size-Controlled Gold–Silver Alloy Nanoparticles. *J. Phys. Chem. C* **2015**, *119*, 13160–13168.
- (4) Poudel, B. K.; Gupta, B.; Ramasamy, T.; Thapa, R. K.; Pathak, S.; Oh, K. T.; Jeong, J.-H.; Choi, H.-G.; Yong, C. S.; Kim, J. O. PEGylated Thermosensitive Lipid-Coated Hollow Gold Nanoshells for Effective Combinational Chemo-Photothermal Therapy of Pancreatic Cancer. *Colloids Surf., B* **2017**, *160*, 73–83.
- (5) Bansal, A.; Sekhon, J. S.; Verma, S. S. Scattering Efficiency of LSPR Tunability of Bimetallic Ag, Au, and Cu Nanoparticles. *Plasmonics* **2014**, *9*, 143–150.
- (6) Gilroy, K. D.; Ruditskiy, A.; Peng, H.-C.; Qin, D.; Xia, Y. Bimetallic Nanocrystals: Syntheses, Properties, and Applications. *Chem. Rev.* **2016**, *116*, 10414–10472.
- (7) Ma, Y.; Liang, X.; Tong, S.; Bao, G.; Ren, Q.; Dai, Z. Gold Nanoshell Nanomicelles for Potential Magnetic Resonance Imaging, Light-Triggered Drug Release, and Photothermal Therapy. *Adv. Funct. Mater.* **2013**, *23*, 815–822.
- (8) Hu, F.; Zhang, Y.; Chen, G.; Li, C.; Wang, Q. Double-Walled Au Nanocage/SiO<sub>2</sub> Nanorattles: Integrating SERS Imaging, Drug Delivery and Photothermal Therapy. *Small* **2015**, *11*, 985–993.
- (9) Antosh, M. P.; Wijesinghe, D. D.; Shrestha, S.; Lanou, R.; Huang, Y. H.; Hasselbacher, T.; Fox, D.; Neretti, N.; Sun, S.; Katenka, N.; Cooper, L. N.; Andreev, O. A.; Reshetnyak, Y. K. Enhancement of Radiation Effect on Cancer Cells by Gold–pHLIP. *Proc. Natl. Acad. Sci. U.S.A.* **2015**, *112*, 5372–5376.
- (10) Tan, K. S.; Cheong, K. Y. Advances of Ag, Cu, and Ag–Cu Alloy Nanoparticles Synthesized via Chemical Reduction Route. *J. Nanopart. Res.* **2013**, *15*, 1537.
- (11) Kitson, P. J.; Marie, G.; Francoia, J.-P.; Zaleskiy, S. S.; Sigerson, R. C.; Mathieson, J. S.; Cronin, L. Digitization of Multistep Organic Synthesis in Reactionware for On-Demand Pharmaceuticals. *Science* **2018**, *359*, 314–319.
- (12) Pfeiffer, T. V.; Feng, J.; Schmidt-Ott, A. New Developments in Spark Production of Nanoparticles. *Adv. Powder Technol.* **2014**, *25*, 56–70.
- (13) Tabrizi, N. S.; Xu, Q.; van der Pers, N. M.; Schmidt-Ott, A. Generation of Mixed Metallic Nanoparticles from Immiscible Metals by Spark Discharge. *J. Nanopart. Res.* **2010**, *12*, 247–259.
- (14) Kim, D.; Resasco, J.; Yu, Y.; Asiri, A. M.; Yang, P. Synergistic Geometric and Electronic Effects for Electrochemical Reduction of Carbon Dioxide Using Gold–Copper Bimetallic Nanoparticles. *Nat. Commun.* **2014**, *5*, 4948.
- (15) Lysgaard, S.; Mýrdal, J. S. G.; Hansen, H. A.; Vegge, T. A DFT-Based Genetic Algorithm Search for AuCu Nanoalloy Electrocatalysts for CO<sub>2</sub> Reduction. *Phys. Chem. Chem. Phys.* **2015**, *17*, 28270–28276.
- (16) He, R.; Wang, Y. -C.; Wang, X.; Wang, Z.; Liu, G.; Zhou, W.; Wen, L.; Li, Q.; Wang, X.; Chen, X.; Zeng, J.; Hou, J. G. Facile Synthesis of Pentacle Gold–Copper Alloy Nanocrystals and their Plasmonic and Catalytic Properties. *Nat. Commun.* **2014**, *5*, 4327.
- (17) Morton, S. W.; Herlihy, K. P.; Shopsowitz, K. E.; Deng, Z. J.; Chu, K. S.; Bowerman, C. J.; DeSimone, J. M.; Hammond, P. T. Scalable Manufacture of Built-to-Order Nanomedicine: Spray-assisted Layer-by-Layer Functionalization of PRINT Nanoparticles. *Adv. Mater.* **2013**, *25*, 4707–4713.
- (18) Karamipour, S.; Sadjadi, M. S.; Farhadyar, N. Fabrication and Spectroscopic Studies of Folic Acid-Conjugated Fe<sub>3</sub>O<sub>4</sub>@Au Core-Shell for Targeted Drug Delivery Application. *Spectrochim. Acta, Part A* **2015**, *148*, 146–155.
- (19) Nair, L. V.; Nagaoka, Y.; Maekawa, T.; Sakthikumar, D.; Jayasree, R. S. Quantum Dot Tailored to Single Wall Carbon Nanotubes: A Multifunctional Hybrid Nanoconstruct for Cellular Imaging and Targeted Photothermal Therapy. *Small* **2014**, *10*, 2771–2775.
- (20) Jhaveri, M. S.; Rait, A. S.; Chung, K. N.; Trepel, J. B.; Chang, E. H. Antisense Oligonucleotides Targeted to the Human  $\alpha$  Folate Receptor Inhibit Breast Cancer Cell Growth and Sensitize the Cells to Doxorubicin Treatment. *Mol. Cancer Ther.* **2004**, *12*, 1505–1512.
- (21) Gupta, B.; Pathak, S.; Poudel, B. K.; Regmi, S.; Ruttala, H. B.; Gautam, M.; Lee, J. S.; Jeong, J.-H.; Choi, H.-G.; Yong, C. S.; Kim, J. O. Folate Receptor-Targeted Hybrid Lipid-Core Nanocapsules for Sequential Delivery of Doxorubicin and Tanespimycin. *Colloids Surf., B* **2017**, *155*, 83–92.
- (22) Meier, R.; Henning, T. D.; Boddington, S.; Tavri, S.; Arora, S.; Piontek, G.; Rudelius, M.; Corot, C.; Daldrup-Link, H. E. Breast Cancers: MR Imaging of Folate-Receptor Expression with the Folate-Specific Nanoparticle P1133. *Radiology* **2010**, *255*, 527–535.
- (23) Ramasamy, T.; Poudel, B. K.; Ruttala, H.; Choi, J. Y.; Hieu, T. D.; Umadevi, K.; Youn, Y. S.; Choi, H.-G.; Yong, C. S.; Kim, J. O. Cationic Drug-Based Self-Assembled Polyelectrolyte Complex Micelles: Physicochemical, Pharmacokinetic, and Anticancer Activity Analysis. *Colloids Surf., B* **2016**, *146*, 152–160.
- (24) Byeon, J. H. Multifunctional Metal-Polymer Nanoagglomerates from Single-Pass Aerosol Self-Assembly. *Sci. Rep.* **2016**, *6*, 31329.
- (25) Zheng, T.; Bott, S.; Huo, Q. Techniques for Accurate Sizing of Gold Nanoparticles Using Dynamic Light Scattering with Particular Application to Chemical and Biological Sensing Based on Aggregate Formation. *ACS Appl. Mater. Interfaces* **2016**, *8*, 21585–21594.
- (26) Zhang, B.; Zhao, W.; Wang, D. Shape-Controlled Self-Assembly of Colloidal Nanoparticles. *Chem. Sci.* **2012**, *3*, 2252–2256.
- (27) Sra, A. K.; Schaak, R. E. Synthesis of Atomically Ordered AuCu and AuCu<sub>3</sub> Nanocrystals from Bimetallic Nanoparticle Precursors. *J. Am. Chem. Soc.* **2004**, *126*, 6667–6672.
- (28) Poudel, B. K.; Kim, J. O.; Byeon, J. H. Photoinduced Rapid Transformation from Au Nanoagglomerates to Drug-Conjugated Au Nanovesicles. *Adv. Sci.* **2018**, *5*, 1700563.
- (29) Yi, Z.; Luo, J.; Tan, X.; Yi, Y.; Yao, W.; Kang, X.; Tang, Y. Mesoporous Gold Sponges: Electric Charge-Assisted Seed Mediated Synthesis and Application as Surface-Enhanced Raman Scattering Substrates. *Sci. Rep.* **2015**, *5*, 16137.
- (30) Vericat, C.; Vela, M. E.; Benitez, G.; Carro, P.; Salvarezza, R. C. Self-Assembled Monolayers of Thiols and Dithiols on Gold: New Challenges for a Well-Known System. *Chem. Soc. Rev.* **2010**, *39*, 1805–1834.
- (31) Xue, Y.; Li, X.; Li, H.; Zhang, W. Quantifying Thiol–Gold Interactions towards the Efficient Strength Control. *Nat. Commun.* **2014**, *5*, 4348.
- (32) Byeon, J. H.; Park, J. H.; Hwang, J. Spark Generation of Monometallic and Bimetallic Aerosol Nanoparticles. *J. Aerosol Sci.* **2008**, *39*, 888–896.
- (33) Zhang, L.; Xu, C.; Song, G.; Li, B. Self-Assembly of L-Cysteine-Gold Nanoparticles as Chiral Probes for Visual Recognition of 3,4-Dihydroxyphenylalanine Enantiomers. *RSC Adv.* **2015**, *5*, 27003–27008.
- (34) Qiao, J.; Mu, X.; Qi, L.; Deng, J.; Mao, L. Folic Acid-Functionalized Fluorescent Gold Nanoclusters with Polymers as Linkers for Cancer Cell Imaging. *Chem. Commun.* **2013**, *49*, 8030–8032.
- (35) Sra, A. K.; Ewers, T. D.; Schaak, R. E. Direct Solution Synthesis of Intermetallic AuCu and AuCu<sub>3</sub> Nanocrystals and Nanowire Networks. *Chem. Mater.* **2005**, *17*, 758–766.
- (36) Huang, P.; Lin, J.; Li, W.; Rong, P.; Wang, Z.; Wang, S.; Wang, X.; Sun, X.; Aronova, M.; Niu, G.; Leapman, R. D.; Nie, Z.; Chen, X. Biodegradable Gold Nanovesicles with an Ultrastrong Plasmonic Coupling Effect for Photoacoustic Imaging and Photothermal Therapy. *Angew. Chem., Int. Ed.* **2013**, *52*, 13958–13964.
- (37) Zha, Z.; Yue, X.; Ren, Q.; Dai, Z. Uniform Polypyrrole Nanoparticles with High Photothermal Conversion Efficiency for Photothermal Ablation of Cancer Cells. *Adv. Mater.* **2013**, *25*, 777–782.
- (38) Liu, S.; Sun, Z.; Liu, Q.; Wu, L.; Huang, Y.; Yao, T.; Zhang, J.; Hu, T.; Ge, M.; Hu, F.; Xie, Z.; Pan, G.; Wei, S. Unidirectional Thermal Diffusion in Bimetallic Cu@Au Nanoparticles. *ACS Nano* **2014**, *8*, 1886–1892.
- (39) Yin, J.; Shan, S.; Yang, L.; Mott, D.; Malis, O.; Petkov, V.; Cai, F.; Shan Ng, M.; Luo, J.; Chen, B. H.; Engelhard, M.; Zhong, C.-J.

Gold–Copper Nanoparticles: Nanostructural Evolution and Bifunctional Catalytic Sites. *Chem. Mater.* **2012**, *24*, 4662–4674.

(40) Mott, D.; Yin, J.; Engelhard, M.; Loukrakpam, R.; Chang, P.; Miller, G.; Bae, I.-T.; Chandra Das, N.; Wang, C.; Luo, J.; Zhong, C.-J. From Ultrafine Thiolate-Capped Copper Nanoclusters toward Copper Sulfide Nanodiscs: A Thermally Activated Evolution Route. *Chem. Mater.* **2010**, *22*, 261–271.

(41) Swiech, O. A.; Opuchlik, L. J.; Wojciuk, G.; Stepkowski, T. M.; Kruszewski, M.; Bilewicz, R. Doxorubicin Carriers Based on Au Nanoparticles – Effect of Shape and Gold-Drug Linker on the Carrier Toxicity and Therapeutic Performance. *RSC Adv.* **2016**, *6*, 31960–31967.

(42) Wang, Y.; Wang, F.; Shen, Y.; He, Q.; Guo, S. Tumor-Specific Disintegratable Nanohybrids Containing Ultrasmall Inorganic Nanoparticles: from Design and Improved Properties to Cancer Applications. *Mater. Horiz.* **2018**, *5*, 184–205.

(43) Poudel, B. K.; Soe, Z. C.; Ruttala, H. B.; Gupta, B.; Ramasamy, T.; Thapa, R. K.; Gautam, M.; Ou, W.; Nguyen, H. T.; Jeong, J.-H.; Jin, S. G.; Choi, H.-G.; Yong, C. S.; Kim, J. O. *In Situ* Fabrication of Mesoporous Silica-Coated Silver–Gold Hollow Nanoshell for Remotely Controllable Chemo-Photothermal Therapy via Phase-Change Molecule as Gatekeepers. *Int. J. Pharm.* **2018**, *548*, 92–103.

(44) Yameen, B.; Choi, W. I.; Vilos, C.; Swami, A.; Shi, J.; Farokhzad, O. C. Insight into Nanoparticle Cellular Uptake and Intracellular Targeting. *J. Controlled Release* **2014**, *190*, 485–499.

(45) Schneider, R.; Schmitt, F.; Frochot, C.; Fort, Y.; Lourette, N.; Guillemain, F.; Müller, J.-F.; Barberi-Heyob, M. Design, Synthesis and Biological Evaluation of Folic Acid Targeted Tetraphenylporphyrin as Novel Photosensitizers for Selective Photodynamic Therapy. *Bioorg. Med. Chem.* **2005**, *13*, 2799–2808.

(46) García-Díaz, M.; Nonell, S.; Villanueva, A.; Stockert, J. C.; Cañete, M.; Casadó, A.; Mora, M.; Sagristá, M. L. Do Folate-Receptor Targeted Liposomal Photosensitizers Enhance Photodynamic Therapy Selectivity? *Biochim. Biophys. Acta* **2011**, *1808*, 1063–1071.

(47) Moret, F.; Scheglmann, D.; Reddi, E. Folate-Targeted PEGylated Liposomes Improve the Selectivity of PDT with Meta-Tetra(Hydroxyphenyl)Chlorin (m-THPC). *Photochem. Photobiol. Sci.* **2013**, *12*, 823–834.

(48) Yang, T.; Xu, F.; Fang, D.; Chen, Y. Targeted Proteomics Enables Simultaneous Quantification of Folate Receptor Isoforms and Potential Isoform-based Diagnosis in Breast Cancer. *Sci. Rep.* **2015**, *5*, 16733.

(49) Sun, Y.; Xia, P.; Zhang, H.; Liu, B.; Shi, Y. p53 is Required for Doxorubicin-Induced Apoptosis via the TGF- $\beta$  Signaling Pathway in Osteosarcoma-Derived Cells. *Am J Cancer Res* **2016**, *6*, 114–125.

(50) Tacar, O.; Sriamornsak, P.; Dass, C. R. Doxorubicin: An Update on Anticancer Molecular Action, Toxicity and Novel Drug Delivery Systems. *J. Pharm. Pharmacol.* **2013**, *65*, 157–170.

(51) Yeudall, W. A.; Vaughan, C. A.; Miyazaki, H.; Ramamoorthy, M.; Choi, M.-Y.; Chapman, C. G.; Wang, H.; Black, E.; Bulysheva, A. A.; Deb, S. P.; Windle, B.; Deb, S. Gain-of-Function Mutant p53 Upregulates CXC Chemokines and Enhances Cell Migration. *Carcinogenesis* **2012**, *33*, 442–451.

(52) Bar-On, O.; Shapira, M.; Hershko, D. D. Differential Effects of Doxorubicin Treatment on Cell Cycle Arrest and Skp2 Expression in Breast Cancer Cells. *Anti-Cancer Drugs* **2007**, *18*, 1113–1121.

(53) Chen, W.-T.; Kang, S.-T.; Lin, J.-L.; Wang, C.-H.; Chen, R.-C.; Yeh, C.-K. Targeted Tumor Theranostics Using Folate-Conjugated and Camptothecin-Loaded Acoustic Nanodroplets in a Mouse Xenograft Model. *Biomaterials* **2015**, *53*, 699–708.

(54) Sunoqrot, S.; Liu, Y.; Kim, D.-H.; Hong, S. In Vitro Evaluation of Dendrimer-Polymer Hybrid Nanoparticles on Their Controlled Cellular Targeting Kinetics. *Mol. Pharmaceutics* **2013**, *10*, 2157–2166.

(55) Huang, S.; Duan, S.; Wang, J.; Bao, S.; Qiu, X.; Li, C.; Liu, Y.; Yan, L.; Zhang, Z.; Hu, Y. Folic-Acid-Mediated Functionalized Gold Nanocages for Targeted Delivery of Anti-miR-181b in Combination of Gene Therapy and Photothermal Therapy against Hepatocellular Carcinoma. *Adv. Funct. Mater.* **2016**, *26*, 2532–2544.

(56) Carvalho, F. S.; Burgeiro, A.; Garcia, R.; Moreno, A. J.; Carvalho, R. A.; Oliveira, P. J. Doxorubicin-Induced Cardiotoxicity: from Bioenergetic Failure and Cell Death to Cardiomyopathy. *Med. Res. Rev.* **2014**, *34*, 106–135.

(57) Yoo, M.-K.; Park, I.-K.; Lim, H.-T.; Lee, S.-J.; Jiang, H.-L.; Kim, Y.-K.; Choi, Y.-J.; Cho, M.-H.; Cho, C.-S. Folate-PEG–Superparamagnetic Iron Oxide Nanoparticles for Lung Cancer Imaging. *Acta Biomater.* **2012**, *8*, 3005–3013.

(58) Zwicke, G. L.; Ali Mansoori, G.; Jeffery, C. J. Utilizing the Folate Receptor for Active Targeting of Cancer Nanotherapeutics. *Nano Rev.* **2012**, *3*, 18496.